International Journal of Fatigue

Infuence of β phase on local deformation pattern in mill-annealed Ti-Fe-O alloy under dwell fatigue loading

--Manuscript Draft--

Manuscript Number:	IJFATIGUE-D-21-00415R2
Article Type:	Original Research Paper
Keywords:	titanium alloy; dwell fatigue; nanoindentation; Crystal plasticity; slip transfer
Corresponding Author:	Osamu Umezawa, Dr Faculty of Engineering Yokohama, Kanagawa JAPAN
First Author:	Liangwei Yin
Order of Authors:	Liangwei Yin
	Osamu Umezawa, Dr
Manuscript Region of Origin:	Asia/Pacific
Abstract:	Grain-scale dwell fatigue behavior in Ti-Fe-O alloy is elucidated, with attention focused on the stress redistribution phenomenon that occurs within the soft-hard grain combination. Elastoplastic properties of the β phase are determined using nanoindentation and crystal plasticity modeling. On this basis, the role of intergranular β lath on stress redistribution is evaluated. Redistribution of stress from the soft to hard α grain is inhibited in the presence of intergranular β lath during dwell period. Meanwhile, the peak stress in the β lath is enhanced. This may result in the competition of two dwell fatigue failure modes at high stress state.
Response to Reviewers:	Thank you very much for your consideration. We hope the response to reviewers is satisfactory and our revised manuscript will be accepted for publication in International Journal of Fatigue.

Highlights

- Load-displacement curves of β single crystal show reasonable agreement between nanoindentation tests and dislocation mechanism-based crystal plasticity modeling.
- Intergranular β lath within the rogue grain combination reduces the dwell fatigue sensitivity of titanium alloys with globular structure.
- Geometrical compatibility of the α/β interface significantly affects the stress redistribution phenomenon.
- Increased peak stress in the intergranular β lath may cause competing dwell fatigue failure modes at the high stress state.

Influence of dispersed β phase on local deformation pattern in mill-annealed Ti-Fe-O alloy under dwell fatigue loading

Liangwei Yin[a], Osamu Umezawa[b,c*]

a. Graduate School of Engineering Science, Yokohama National University

b. Faculty of Engineering, Yokohama National University

c. Center of Advanced Innovation Technologies, Vysoká Škola Báňská - Technical University of Ostrava

*Corresponding author: Osamu Umezawa (umezawa-osamu-fv@ynu.ac.jp)

Abstract

Grain-scale dwell fatigue behavior in Ti-Fe-O alloy is elucidated, with attention focused on the stress redistribution phenomenon that occurs within the soft-hard grain combination. Elastoplastic properties of the β phase are determined using nanoindentation and crystal plasticity modeling. On this basis, the role of intergranular β lath on stress redistribution is evaluated. Redistribution of stress from the soft to hard α grain is inhibited in the presence of intergranular β lath during dwell period. Meanwhile, the peak stress in the β lath is enhanced. This may result in the competition of two dwell fatigue failure modes at high stress state.

Keyword: titanium alloy; dwell fatigue; nanoindentation; crystal plasticity; slip transfer

1. Introduction

Near-α and α/β titanium alloys have been extensively used to manufacture rotor components in the cold section of high-bypass turbofan engines, such as fan and compressor discs, owing to their advantages such as high specific strength, fracture toughness and excellent corrosion resistance. In these specific applications, premature fatigue failure, termed "dwell fatigue life debit", occurs in titanium alloy components subjected to dwell fatigue loading with a static high mean stress hold in each cycle at ambient temperatures [1]. The fatigue life reduction presumably results from the formation of near basal facets within subsurface fatigue crack initiation sites [2], [3]. Facet nucleation is closely associated with the micromechanical deformation behaviors at the grain scale. A rogue grain combination comprising soft (well oriented for slip) and hard (poorly oriented for slip) α grains has been predicted to be the most detrimental site for dwell facet generation according to the stress redistribution model, that is, the soft grain sheds stress onto the hard grain due to the cold creep deformation during the dwell period [1].

The cold creep ($T < 0.3T_m$), which causes stress redistribution and concentration in dwell fatigue, occurs principally through dislocation slip. For dual-phase titanium alloys, the slip activities are strongly dependent on the α/β phase morphology. Ashton et al. [4] noted that soft $\alpha+\beta$ colonies in the bimodal microstructure could release the stress concentration in adjacent hard primary α grains since the presence of β laths shortened the slip length and reduced the dislocation pile-ups at hard-soft grain boundaries after stress dwell. Soft basketweave structure has also been reported to inhibit slip accumulation during dwell time because of the distinct soft α laths formed inside the β matrix [5]. These assumptions are consistent with the experimental results that titanium alloys with lamellar or basketweave structures are less susceptible to dwell fatigue life reduction [6]. In addition to the aforementioned microstructures, α laths in lamellar colonies can be spheroidized through dynamic recrystallization to achieve a globular structure with β at α grain boundaries. The resulting morphologies of the α phase within the globular structure are equiaxed α grains or elongated α platelets depending on the hot deformation and heat treatment processing parameters. Dwell fatigue tests have also been

conducted for α/β titanium alloys with this practical microstructure. A comparison of the dwell fatigue life debit of Ti-6Al-2Sn-4Zr-xMo (Ti-624x, x = 2-6) alloys with equiaxed α grains suggested that the dwell sensitivity of Ti-624x faded out as the addition of Mo could refine the size of primary α grains and reduce slip band spacing [7]. This study highlighted the role of the α phase, the concurrent growth of the intergranular β phase volume fraction was not taken into account. The deviation from the Burgers orientation relationship (BOR) between the α and β phase after the dynamic recrystallization process could block the slip transfer at the α/β interface, as well as dislocation interactions [8]. On the other hand, β laths decorating two geometrically incompatible equiaxed α grains were capable of coordinating regional deformation by continuous slip transmission under certain crystallographic orientation relationships [9]. However, most of the previous studies on the intergranular β phase have focused on deformation mechanisms under monotonic loading, the effect of intergranular β phase on the creep resistance and dwell fatigue sensitivity remains elusive in near-α and α/β titanium alloys with globular structure.

Elucidating the effect of the β phase necessitates the calibration of its elastoplastic properties such as elastic stiffness constants and critical resolved shear stress (CRSS). The small volume fraction of the β phase in near-α and α/β titanium alloys makes it difficult to extract these datasets from bulk materials. Consequently, micro-scale mechanical tests were developed for accurate measurements in a single phase. The nanoindentation technique was used to probe the nanohardness in a dual-phase Ti-15Mo-Fe alloy and β phase was determined to be harder than α phase [10]. In addition to performing the strength assessment, Jun et al. [11] compared the local strain-rate sensitivity (SRS) in Ti-6242 and Ti-6246 alloys by nanoindentation using the constant stiffness measurement (CSM) method, and assumed that the difference in SRS was attributed to increased thickness of β ligaments as a result of Mo addition. Furthermore, Zhang et al. [12] combined micropillar compression tests and crystal plasticity modeling to determine the slip property of the β phase in Ti-6242 alloy with lamellar structure. Nevertheless, due to the addition of various β-stabilizing alloying elements (e.g., Mo, V, Nb, Cr, Fe, and Ta), the intrinsic properties of β phase exhibit notable composition dependence [13]. For instance,

the elastic modulus of the β phase varies widely from 60 to 110 GPa, and the CRSS of slip systems ranges from 201 to 387 MPa [13], [14]. Therefore, it is imperative to examine the micro-elastoplasticity of the β phase in Ti-Fe-O alloy.

This study aims to evaluate the effect of the β phase on the local deformation behaviors in mill-annealed Ti-Fe-O alloy under dwell fatigue loading. First, constant stiffness measurement nanoindentation tests and dislocation mechanism-based crystal plasticity finite element (CPFE) simulations are performed to identify the elastoplastic parameters of the β phase. The data of the α phase are also calibrated via a series of macroscopic mechanical tests. Then, based on the examination of the dwell fatigue failure modes, a polycrystalline aggregate model is established using Voronoi tessellation to investigate the stress redistribution procedure in the rogue grain combination containing the intergranular β lath. A geometrical compatibility factor is employed to link the dislocation pile-ups at the α/β interfaces and stress redistribution in terms of the resistance against slip transfer. On the basis of the proposed relationship and analysis of crystallographic orientation in Ti-Fe-O alloy, the influence of β lath thickness on the dwell fatigue sensitivity and two load-dependent competing crack initiation modes are discussed.

2. Experimental procedure

2.1 Material

The main chemical compositions of the tested near-α Ti-Fe-O alloy (Nippon Steel Corporation) are as follows: 0.994 Fe, 0.386 O, 0.003 N, 0.003C, 0.0005 H, and balance of Ti in mass% [15]. In this alloy, O and Fe are respectively used as α and β stabilizers for cost reduction. The Ti-Fe-O alloy was double-melted in vacuum arc remelting, forged (1273 K heating), and hot rolled (1123 K heating) along the rolling direction (RD) to an 80-mm-thick plate. The 80-mm-thick plate was cross-rolled (1123 K heating) along the transverse direction (TD) to a 33-mm-thick plate. Thereafter, the plate was annealed at 1023 K for 1 h, and subsequently air cooled. This thermomechanical processing route resulted in a typical mill-annealed microstructure containing primary α grains (light region) with a certain elongation along RD and transformed β phase (dark region) at the α grain boundaries, as shown in **Fig. 1(a) and (b)**. The average size of the primary α grain

shrinks to 35 μm in diameter as the addition of Fe accelerates heterogeneous grain nucleation. According to Fig. 1(b), the thickness of β lath approximately ranges from 0.5 μm to 2 μm. A sample with dimensions of 10 mm × 5 mm × 1 mm was prepared for nanoindentation tests. In addition, flat dog-bone specimens with gauge sections of 30 mm long, 5 mm wide, and 2 mm thick were machined parallel to RD for quasi-static tensile, stress relaxation and dwell fatigue tests.

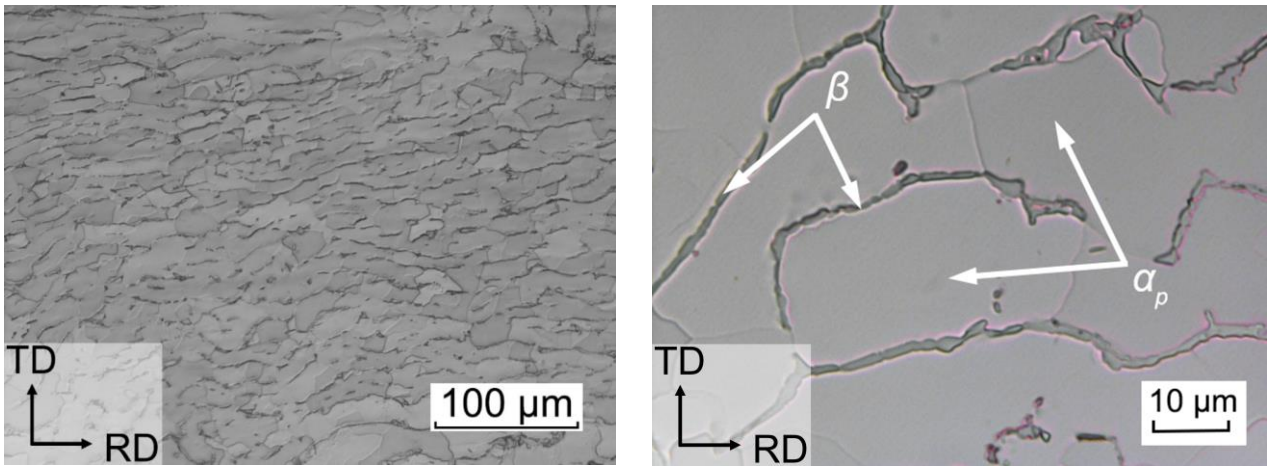

(a) (b)

Fig. 1 (a) Optical microstructure of Ti-Fe-O alloy on the ND plane, (b) intergranular β phase at primary α (α_p) grain boundaries.

Prior to mechanical tests, the specimens were first polished using SiC papers (<#2400) and electropolished at -40 ℃ for 35 s in a solution of methanol (440 mL), butanol (264 mL), and $HClO_4$ (44 mL). Electron back-scattered diffraction (EBSD) measurements were then conducted using a JEOL JSM-7100F scanning electron microscope (SEM) operating at an accelerating voltage of 15 kV equipped with a TSL™ EBSD detector. The step size of EBSD scan was 0.5 μm, and raw data were analyzed using the TSL OIM analysis 7 software and MTEX toolbox in MATLAB [16].

2.2 Mechanical tests

To perform micromechanical characterization of the β phase, nanoindentation tests were conducted using Hysitron Ti-750 TriboIndenter equipped with a Berkovich diamond indenter. The loading/unloading procedures comprised three stages: displacement-controlled loading to a maximum depth of 250 nm using the CSM method, 10 s holding, and 20 s unloading. The indentation strain rate $\dot{\varepsilon}$ in the CSM method is expressed as follows [17]

$$\dot{\varepsilon}=\frac{\dot{h}}{h}\approx\frac{1}{2}\frac{\dot{P}}{P} \tag{1}$$

where h and $\dot{h}$ are the displacement and corresponding rate, P and $\dot{P}$ are the indentation load and loading rate, respectively. The experimental indentation strain rates were set to 0.05 s^{-1} and 0.1 s^{-1} to investigate the SRS of the β phase, which is linked to the creep deformation during dwell fatigue.

The macroscopic responses of near-α and α/β titanium alloys are barely influenced by the minor β phase during deformation, therefore, macroscopic mechanical tests were performed to calibrate the crystal plasticity parameters of the α phase [13]. Quasi-tensile tests were performed on a motor-driven tester (SHIMAZU AG-IS 20kNT) under three strain rates ($8.3\times10^{-4}\ s^{-1}$, $8.3\times10^{-3}\ s^{-1}$, $8.3\times10^{-2}\ s^{-1}$) to obtain stress-strain curves at 298 K. Slip trace analysis was implemented on one specimen tested at the strain rate of $8.3\times10^{-4}\ s^{-1}$ to identify the operating slip systems in the α phase and determine the CRSS relationships. In this procedure, the active slip trace was designated as the slip system with the highest global Schmid factor (SF). In addition, stress relaxation test, which interrupted the tensile tests at 540 MPa by a 300 s stress relaxation period followed by unloading, was also carried out to further calibrate the SRS parameters of the α phase.

Load-controlled dwell fatigue tests were carried out at room temperature (298K). The dwell fatigue load was applied in a trapezoidal waveform with a loading/unloading time of 1 s and a dwell time of 120 s at the peak stress. The peak stresses were 602 MPa (0.95 σ_y at $8.3\times10^{-4}s^{-1}$) and 538 MPa (0.85 σ_y at $8.3\times10^{-4}s^{-1}$) to investigate the effect of stress level on the fatigue crack initiation behavior. The stress ratio R was set to 0.01.

3. Crystal plasticity finite simulation framework

3.1 Crystal plasticity constitutive model

The rate-dependent crystal plasticity framework used in this study was originally developed by Huang based on the finite strain theory [18]. The deformation gradient $\boldsymbol{F}$ is given by

$$\boldsymbol{F}=\boldsymbol{F}^{e}\cdot\boldsymbol{F}^{p} \tag{2}$$

where $\boldsymbol{F}^{e}$ refers to the lattice stretching and rigid body rotation, and $\boldsymbol{F}^{p}$ denotes the deformation caused by the plastic

shear of the material.

Eq. (2) can be used to develop the following equation, which is based on the additive decomposition of the velocity gradient $\boldsymbol{L}$ into elastic and plastic parts,

$$\boldsymbol{L} = \dot{\boldsymbol{F}} \cdot \boldsymbol{F}^{-1} = \dot{\boldsymbol{F}}^{e} \cdot (\boldsymbol{F}^{e})^{-1} + \boldsymbol{F}^{e} \cdot \dot{\boldsymbol{F}}^{p} \cdot (\boldsymbol{F}^{p})^{-1} \cdot (\boldsymbol{F}^{e})^{-1} = \boldsymbol{L}^{e} + \boldsymbol{F}^{e} \cdot \boldsymbol{L}^{p} \cdot (\boldsymbol{F}^{e})^{-1} \tag{3}$$

Assuming that the plastic deformation results from all active slip systems,

$$\boldsymbol{L}_{p} = \sum_{i=1}^{n} \dot{\gamma}^{i} (\boldsymbol{m}^{i} \otimes \boldsymbol{s}^{i}) \tag{4}$$

where n is the total number of slip systems, $\dot{\gamma}^{i}$ is the shearing rate of the ith slip system, $\boldsymbol{m}^{i}$ and $\boldsymbol{s}^{i}$ are the slip plane normal and slip direction, respectively.

For the α phase with hexagonal close-packed (HCP) lattice, five active slip system families, including 3 $(0001)\langle 11\bar{2}0\rangle$ basal, 3 $(10\bar{1}0)\langle 11\bar{2}0\rangle$ prismatic, 6 $(10\bar{1}1)\langle 11\bar{2}0\rangle$ pyramidal, 12 $(10\bar{1}1)\langle 11\bar{2}3\rangle$ 1st pyramidal, and 6 $(11\bar{2}2)\langle 11\bar{2}3\rangle$ 2nd pyramidal slip systems, are taken into account. Since the plastic deformation carried by deformation twinning is considerably suppressed by high oxygen content (mass% O > 0.11), the twinning activity in α phase is ignored [19]. The body-centered cubic (BCC) β phase consists of 12 $\{110\}\langle 111\rangle$ and 12 $\{112\}\langle 111\rangle$ slip systems. Since the activation of the $\{123\}\langle 111\rangle$ slip is difficult, this family is not considered without affecting results significantly [8], [20]. The shearing rate $\dot{\gamma}^{i}$ on slip system i follows a thermally activated model considering forward and backward dislocation activation events [21]:

$$\begin{cases} \dot{\gamma}^{i} = 0 & \text{if } \left|\tau^{i}\right| \le \tau_{c}^{i} \\ \dot{\gamma}^{i} = \rho_{m} (b_{i})^{2} \upsilon_{D} \exp(-\dfrac{\Delta F}{kT}) \sinh(\dfrac{(\left|\tau^{i}\right| - \tau_{c}^{i}) \Delta V}{kT}) & \text{if } \left|\tau^{i}\right| \ge \tau_{c}^{i} \end{cases} \tag{5}$$

where ρ_{m} is the mobile dislocation density, b_{i} is the Burgers vector, υ_{D} is the Debye frequency, k is the Boltzmann constant, and T is the temperature. ΔF and ΔV are the activation energy and activation volume, respectively, which significantly influence the SRS of slip systems. τ^{i} is the resolved shear stress and τ_{c}^{i} is the effective CRSS.

Based on the strain-gradient crystal plasticity framework developed by Han et al. [22], the effective CRSS τ_{c}^{i} of slip

system *i* takes the contribution of statistically stored dislocations (SSDs) and geometrically necessary dislocations (GNDs) into consideration [23]:

$$\tau_i^c = \sqrt{(\tau_{SSD}^i)^2 + (\tau_{GND}^i)^2} \tag{6}$$

where τ_{SSD}^i and τ_{GND}^i are the slip strengths caused by the SSDs and GNDs, respectively. The Voce-type hardening model is applied to describe the evolution of τ_{SSD}^i [24]:

$$\dot{\tau}_{SSD}^i = \sum_{j=1}^n h_{ij} \left| \dot{\gamma}^j \right| \tag{7}$$

where h_{ij} is the hardening moduli, which stands for the interaction among slip systems. The self-hardening moduli h_{ii} and latent hardening moduli h_{ij} are expressed as follows:

$$h_{ii} = h(\gamma) = h_0 (1 - \frac{\tau_0}{\tau_\infty}) \exp(-\frac{h_0 \gamma}{\tau_\infty}),\ \gamma = \sum_{i=1}^n \int_0^t \left| \dot{\gamma}^j \right| dt,\ h_{ij} = q h(\gamma) \tag{8}$$

where h_0, τ_∞, and τ_0 are the initial hardening modulus, saturated CRSS and initial CRSS, respectively. γ is the cumulative shear strain on all slip systems, and q is the latent hardening constant.

The intrinsic length scale of the material, l, is introduced to account for the GND-induced hardening:

$$l = \frac{\alpha_T^2 G^2 b}{(g_0)^2} \tag{9}$$

where α_T is an empirical coefficient, G is the shear modulus, and g_0 is the reference slip resistance, which is expressed as $g_0 = G/100$. The slip strength due to the accumulation of GNDs is then computed based on the Taylor dislocation model [25],

$$\tau_{GND}^i = g_0 \sqrt{l \rho_{GND}^i} = \alpha_T G \sqrt{b_i \rho_{GND}^i} \tag{10}$$

where ρ_{GND}^i is the effective density of GNDs, which has the following form at small deformations:

$$\rho_{GND}^i = \left| \frac{\partial \gamma^i}{\partial \boldsymbol{x}} \right| = \left| \boldsymbol{m}^i \times \sum_{j=1}^n [(\boldsymbol{s}^i \cdot \boldsymbol{s}^j) \nabla \boldsymbol{\gamma}^j \times \boldsymbol{m}^j] \right| \tag{11}$$

The calculation of the effective density of GNDs requires the evaluation of the shear strain gradient at each element integration point, which is summarized in Ref. [26]. Using Eqs. (6) and (10), the effective CRSS of slip system *i* can be rewritten as:

$$\tau_c^i = \sqrt{(\tau_{SSD}^i)^2 + (\alpha_T G)^2 b_i \rho_{GND}^i} \tag{12}$$

The code of the crystal plasticity model is scripted in the UMAT and URDFIL subroutines incorporated within ABAQUS.

3.2 Finite element simulation

The grain size distribution, grain boundary misorientation angle distribution, and crystallographic orientations for the α phase of Ti-Fe-O alloy, as given in **Fig. 2(a)-(c),** are obtained from EBSD measurement and imported into an open-source software Dream.3D to generate a cuboidal representative volume element (RVE) comprising 147 globular α grains, as shown in Fig. 2(d) [27]. Considering the effect of the β phase on the macroscopic responses can be neglected due to the limited volume fraction (~8%), the pure α phase RVE model is used to produce numerical stress-strain and stress relaxation curves. [28]. The RVE is meshed by 32768 C3D8 fully integrated solid elements. The x, y and z directions represent the TD, RD and normal direction (ND), respectively. Uniform displacement is imposed along the RD.

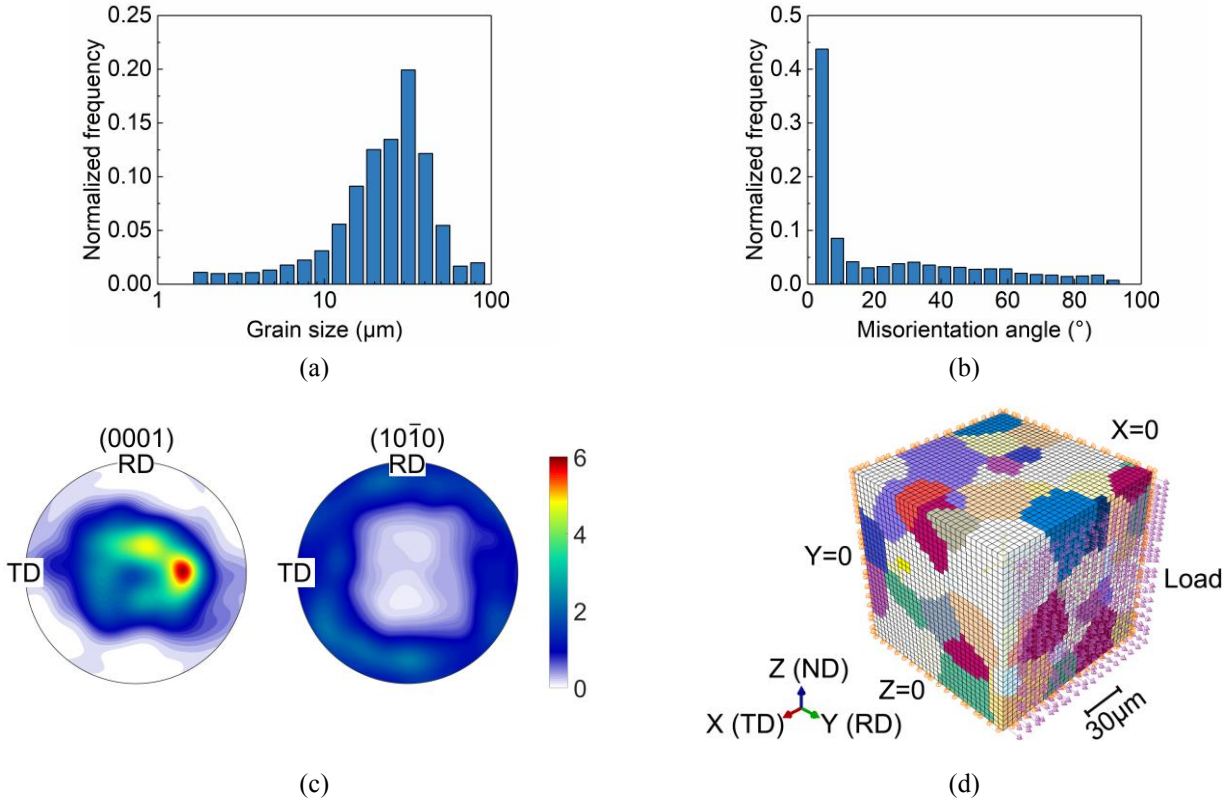

Fig. 2 (a) Grain size distribution, (b) grain boundary misorientation distribution, (c) pole figure of the α phase in Ti-Fe-O alloy and (d) resulting representative volume element.

A three-dimensional model, which consisted of a single crystal with dimensions of 5 μm × 5 μm × 3 μm and a rigid

Berkovich indenter with a sharp tip, is constructed for nanoindentation simulation, as shown in **Fig. 3**. The single crystal and indenter are meshed by 26944 C3D8 elements and 180 R3D4 discrete rigid elements, respectively. All freedoms of the bottom surface are fixed, and the contact surface is assumed to be frictionless [29]. It has to be mentioned that the crystal orientation is assigned as the average value of original orientations in a grain.

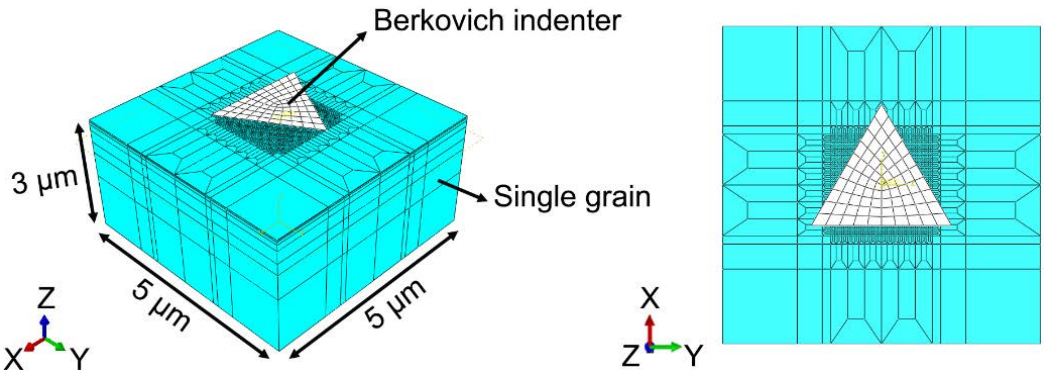

Fig. 3 Nanoindentation finite element model.

A quasi-3D polycrystalline aggregate model is extruded from 2D Voronoi tessellation to study the stress redistribution between hard and soft grains during dwell fatigue, as shown in **Fig. 4**. The basic model is meshed by 15740 C3D8 elements, and the element size is refined within a rogue grain combination in the central area. Soft grains with prismatic SF of 0.5 ($\theta = 15^{\circ}$) can result in the most severe condition for facet nucleation [30]. The crystalline orientations of the surrounding grains are randomly generated. The normal displacements of the left, bottom and back surfaces are fixed to eliminate rigid body movements. A dwell fatigue cycle is applied on the top surface with a maximum stress of 602 MPa and hold time of 120 s. Based on this pure α polycrystalline model, β laths with two thicknesses are explicitly inserted into the hard-soft grain boundary to investigate the effect of the β phase on the stress redistribution during the stress-dwell period, as shown in **Fig. 5**. The thickness of the β lath in **Fig. 5(a)** is 1.8 μm, which is near the upper limit of the thickness range in **Fig. 1(b)**, while the thin β lath with thickness of 0.75 μm in **Fig. 5(b)** is close to the lower limit.

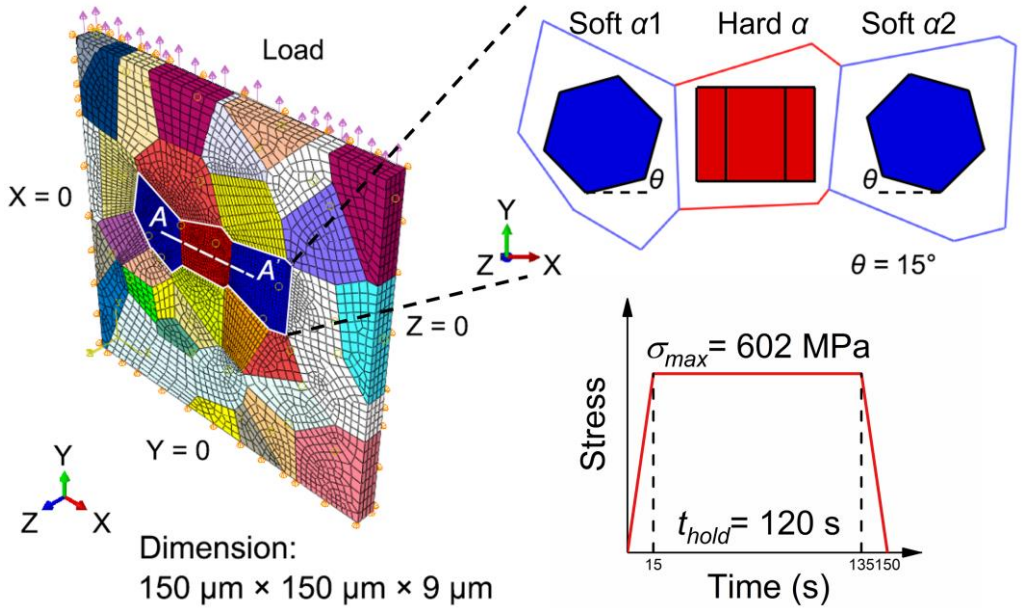

Fig. 4 Polycrystalline aggregate model with a rogue grain combination at the center region, and corresponding loading condition.

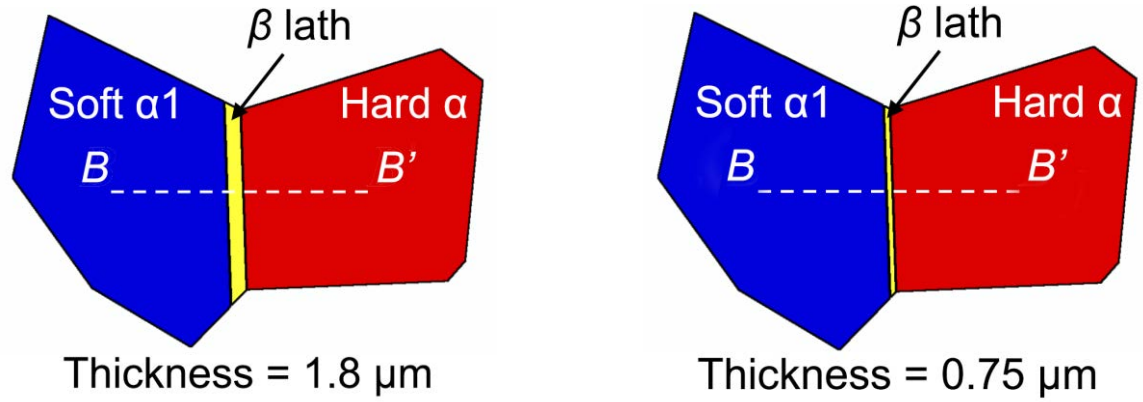

(a) (b)

Fig. 5 Intergranular β lath between soft and hard α grains with thicknesses of (a) 1.8 μm and (b) 0.75 μm.

4. Results and discussion

4.1 Parameter identification

To numerically reproduce the experimental results, the crystal plasticity parameters of the α and β phases should be calibrated. The anisotropic elastic stiffness matrix of the α phase is referred to Ref. [31]. Since the elastic anisotropy of β phase varies dramatically due to different compositions, the isotropic elastic β phase is assumed in this study. The Young's modulus of β phase is measured by nanoindentation tests [29], Poisson's ratio is set to be 0.34.

With respect to the parameters related to the SRS property, the mobile dislocation density ρ_m, Burgers vector b_i, and

Debye frequency υ_D in Eq. (5) are referred to Ref. [4], whereas the activation energy ΔF and activation volume ΔV are determined via calibration. For the α phase in Ti-Fe-O alloy, the CRSS relationships in the Ti-O system are applied since no Fe is observed within the α phase according to our previous energy-dispersive X-ray spectroscopy (EDS) chemical microanalysis [32]. For the Ti-O system, prismatic slip is generally recognized as the most active slip system. By contrast, the CRSS value of basal slip is the highest [33]. $CRSS_{pyramidal<a>} / CRSS_{prismatic}$ decreases with increasing oxygen content in light of the slip trace analysis conducted by Morita et al. [34]. Thus, $CRSS_{pyramidal<a>} / CRSS_{prismatic}$ in Ti-Fe-O alloy can be extrapolated from this relationship. Similarly, pyramidal <*c*+*a*> slip can also be promoted with the addition of oxygen to achieve homogeneous deformation along *c*-axis as substitutions of deformation twinning [35]. Based on previous studies, the CRSS rank of the α phase in ascending order is prismatic, pyramidal <*a*>, pyramidal <*c*+*a*> and basal slip. In addition, given the fact that atomic size difference between Fe and Ti enables substantial solution strengthening, the slip strength of β phase in Ti-Fe-O alloy is assumed to be higher than that of prismatic slip in the α phase [14], [36]. The slip-dependent strain-hardening parameters are calibrated using the curve-fitting method.

The crystal plasticity parameters for the α and β phases are summarized in **Tables 1-2**. The activation energy ΔF and activation volume ΔV for the β phase are smaller than those of the α phase. This trend is similar to the results of Zhang et al. and implies that the β phase is more rate sensitive than the α phase [12]. The CRSS ratio of the α phase is 1: 1.67: 2.5: 2.5: 3 for the prismatic: pyramidal <*a*>: 1st pyramidal <*c*+*a*>: 2nd pyramidal <*c*+*a*>: basal slip systems. The CRSS ratio of $\langle 11\bar{1} \rangle$ slip to prismatic slip is 1.4. Besides, the latent hardening constant in Eq. (8) is assumed to be $q = 1$ for all slip systems, and the empirical coefficient α_T in Eq. (9) is set to 0.7 [37].

Table 1 Elastic constants for α and β phases.

α phase					β phase	
C_{11} (GPa)	C_{22} (GPa)	C_{12} (GPa)	C_{13} (GPa)	C_{44} (GPa)	E (GPa)	ν
162.4	180.7	92.0	69.0	46.7	98	0.34

Table 2 Rate-sensitive and strain gradient parameters for the Ti-Fe-O alloy.

Parameters		α phase	β phase
Rate sensitivity	ρ_m (μm^{-2})	5	
	υ_D (Hz)	1×10^{11}	
	k (J/K)	1.38×10^{-23}	
	b (μm)	0.295 (<*a*> slip)	0.332
		0.468 (<*c*+*a*> slip)	
	ΔF (eV)	0.5194	0.4758
	ΔV	$14.97b^3$	$3.56b^3$
Strain gradient	α_T	0.7	
	G (MPa)	44230	

Table 3 CRSS and strain-hardening parameters for slip systems, in MPa.

	α phase					β phase
	Basal <*a*>	Prism <*a*>	Pyramidal <*a*>	1st Pyramidal <*c*+*a*>	2nd Pyramidal <*c*+*a*>	$\langle 111 \rangle$
h_0	500	150	150	450	450	300
τ_∞	850	328	570	718	718	455
τ_0	636	212	354	530	530	297

4.2 Macroscopic and microscopic responses

The results of quasi-static tensile, stress relaxation tests and accompanying crystal plasticity simulations are plotted in **Fig. 6(a) and (b)**. The responses of the RVE model closely matches the experimental results. The macroscopic yield strength and ultimate tensile strength of the tested Ti-Fe-O alloy is lower than those of Ti-6Al-4V and Ti-6242 at room temperature. Thus, the prismatic CRSS value of the α phase in Ti-Fe-O alloy is relatively small. Furthermore, the quantitative analysis of slip trace in α phase is given in **Fig. 7**. The results indicates that plastic deformation is dominated by prismatic slip, followed by pyramidal <*a*> slip, pyramidal <*c*+*a*> slips and negligible $\{10\bar{1}2\}$ tension twinning,

whereas basal slip is not observed. Hence, the identification of the CRSS relationship is validated to be reasonable. In addition, although the <*a*>-basal dislocation pile-ups in soft grains is reported to generate more stress redistribution than <*a*>-prismatic dislocation in Ti-6242, the current work only focuses on the latter since the nucleation of <*a*>-basal dislocation in Ti-Fe-O alloy is difficult, as shown in **Fig. 4** [38].

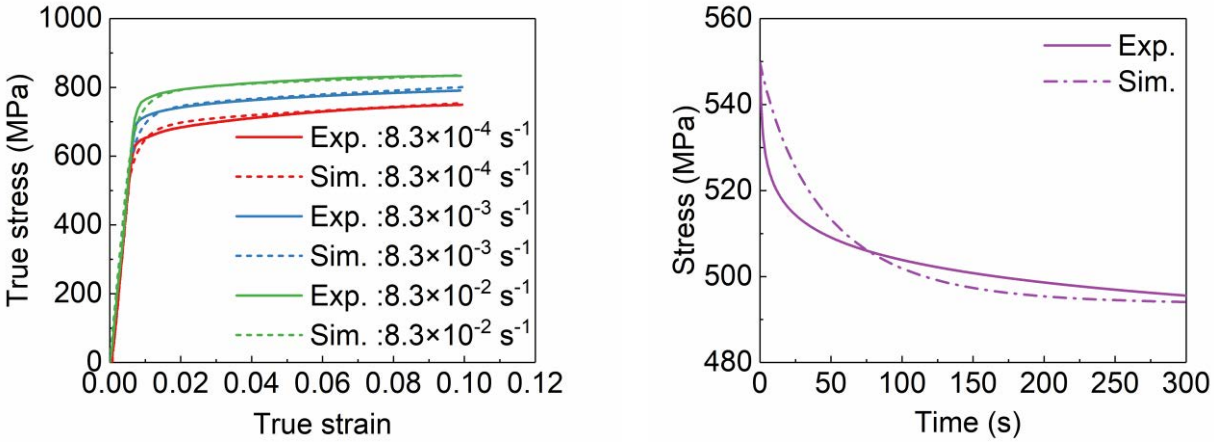

(a) (b)

Fig. 6 Macroscopic responses obtained from (a) tensile, (b) stress relaxation tests.

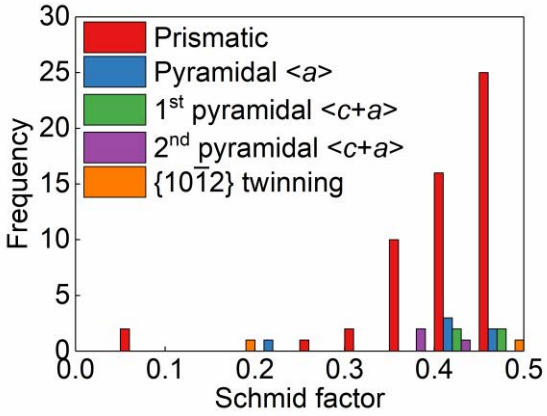

Fig. 7 Histogram of the Schmid factor distribution of different deformation modes in α phase at 3% strain.

The SEM images and relevant inverse pole figure (IPF) maps for two β ($\beta1$ and $\beta2$) and neighboring α grains after nanoindentation tests, together with corresponding experimental and numerical load-displacement curves, are plotted in **Fig. 8**. Two β grains with relatively coarse sizes are selected to ensure the experimental results can precisely reflect the intrinsic properties of the β phase without the influence of surrounding α/β grain boundaries. Grain $\beta1$ is used to calibrate the parameters of the β phase and validation is carried out on grain $\beta2$. Six indentations are

numbered from 1 to 6. Among those, indentations 1 (3) and 2 (4) are tested on the two β grains at indentation strain rates of 0.05 s^{-1} and 0.1 s^{-1}, respectively. Indentations 5 and 6 are tested on the soft α grain. The load-displacement curves of the β phase obtained from the nanoindentation tests are faithfully reproduced by numerical computations, as shown in **Fig. 8(a) and (b)**. Although the single crystal finite element model cannot precisely reflect the local grain morphology, the distances from indentations to grain boundary are sufficiently large such that the influence of grain boundary on load-displacement curves is trivial [39]. The mean Young's modulus of the β phase is measured to be 98 GPa since interaction of Fe with interstitial O, referred to Snoek effect, can pronouncedly increase the elastic stiffness [14]. It should be noted that the effect of size on intrinsic properties of the β phase is insignificant within a few microns, the calibrated parameters are therefore considered to be adequate for thin intergranular β phase, as the β laths modeled in the polycrystalline aggregate model **(Fig. 5)** [12], [40]. Moreover, the load-displacement curves obtained by nanoindentation tests on the soft α grain (**Fig. 8(a)**) are also predicted by simulations with a sound accuracy, as shown in **Fig. 9**, which demonstrates that the material parameters of the α phase calibrated by macroscopic responses are reasonable.

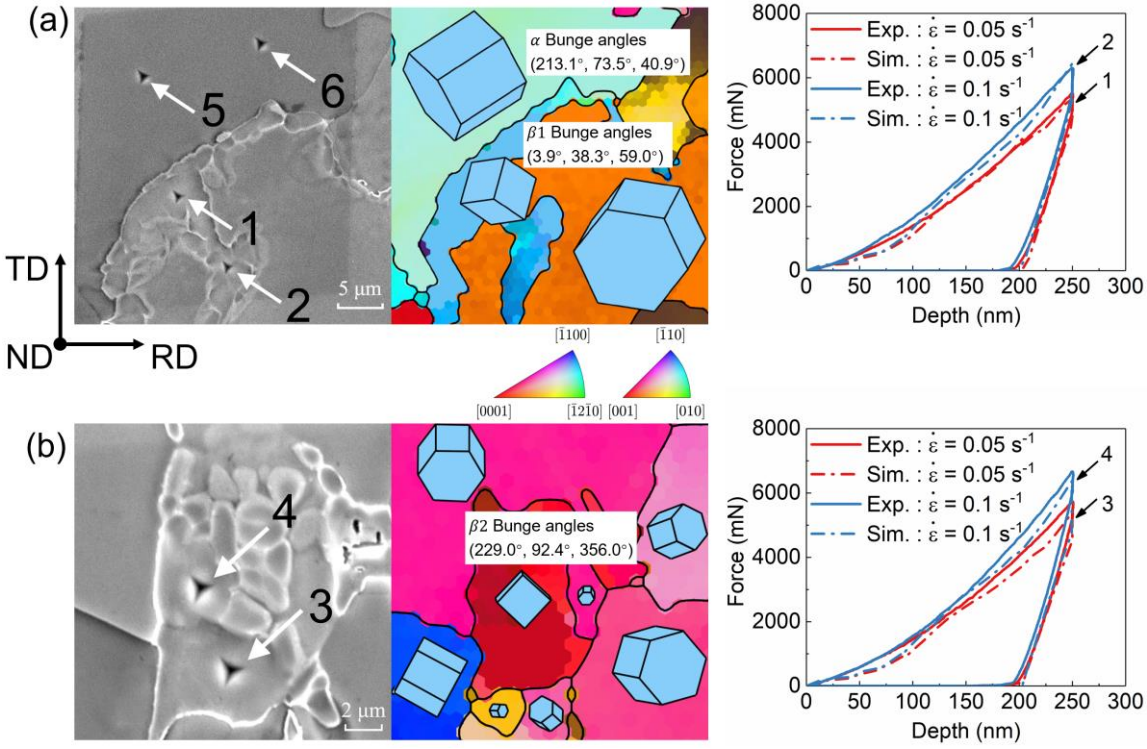

Fig. 8 SEM micrographs with indentations, related IPF maps of ND, and load-displacement curves for nanoindentations of (a) grain $\beta 1$, (b) grain $\beta 2$.

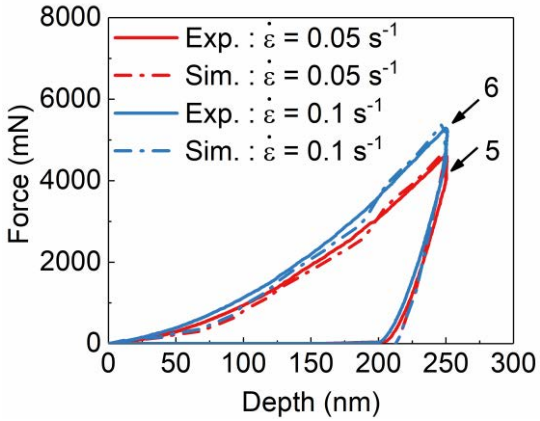

Fig. 9 Load-displacement curves for nanoindentation of the soft α grain shown in Fig. 8(a).

4.3 Fatigue life and crack initiation mode

The comparison of the results between dwell fatigue tests and normal cyclic fatigue tests are summarized in **Fig. 10** [41]. Conspicuous reduced lives can be seen under dwell fatigue loading. The dwell fatigue life debit (ratio of the normal cyclic fatigue life to dwell fatigue life) increases from 13.8 at $\sigma_{max} = 538$ MPa to around 30 at $\sigma_{max} = 602$ MPa. This trend is identical to previous experimental results that dwell fatigue life debit increases with increasing stress level [1]. The fracture surface of the failed sample at $\sigma_{max} = 538$ MPa is illustrated in **Fig. 11(a) and (b)**. The subsurface crack initiation site is about 40 μm from the surface and demonstrates planar facet. Moreover, a large number of subsurface cavities are observed to form in the intergranular β laths of the failed sample at $\sigma_{max} = 602$ MPa, as shown in **Fig. 12(a)-(d)**. It should be mentioned that although the two hard α grains are respectively tilted 53° (**Fig. 12(b)**) and 24° (**Fig. 12(d)**) from loading direction and result in high basal SF, the onset of plastic slip is still difficult concerning the high CRSS of basal slip and low prismatic SF. According to **Fig. 12(a) and (c)**, both quasi-crack cavities (C1 and C5) are within the rogue grain combination and nearly perpendicular to the loading direction. In particular, only the cavities (C1, C5) initiated in the intergranular β laths of rogue grain combination can propagate into neighboring α grains, while the nucleated cavities (C3, C4, C6, and C7) in intergranular β laths sandwiched between two soft α

grains cannot break the α/β interface. Therefore, the intergranular β phase is likely to play an important role on dwell fatigue behavior at high stress state and the influence will be discussed in the following sections.

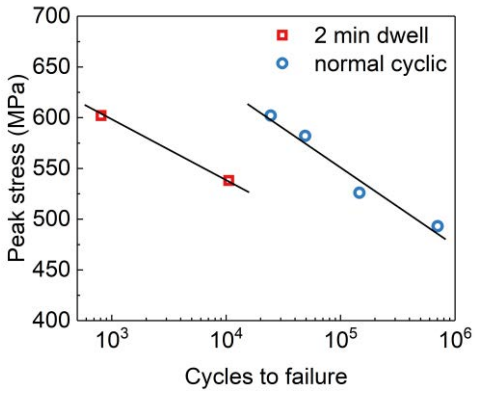

Fig. 10 Fatigue experimental results of dwell fatigue tests and normal cyclic fatigue tests. The normal cyclic fatigue life data can be found in Ref. [41].

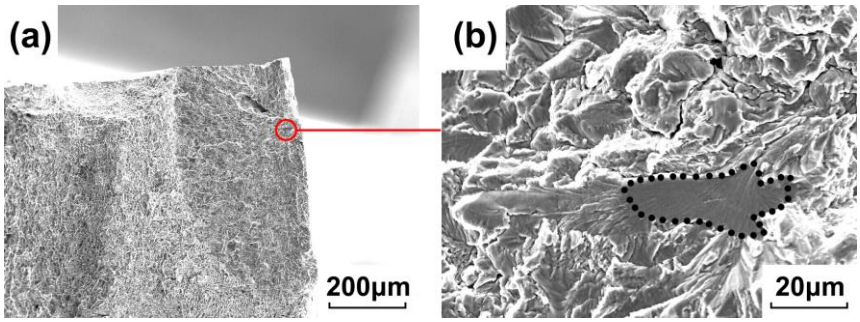

Fig. 11 Fracture surface of the failed sample at $\sigma_{max} = 538$ MPa: (a) low magnification (encircled region indicates the fatigue crack initiation site) (b) high magnification of crack initiation site with facet.

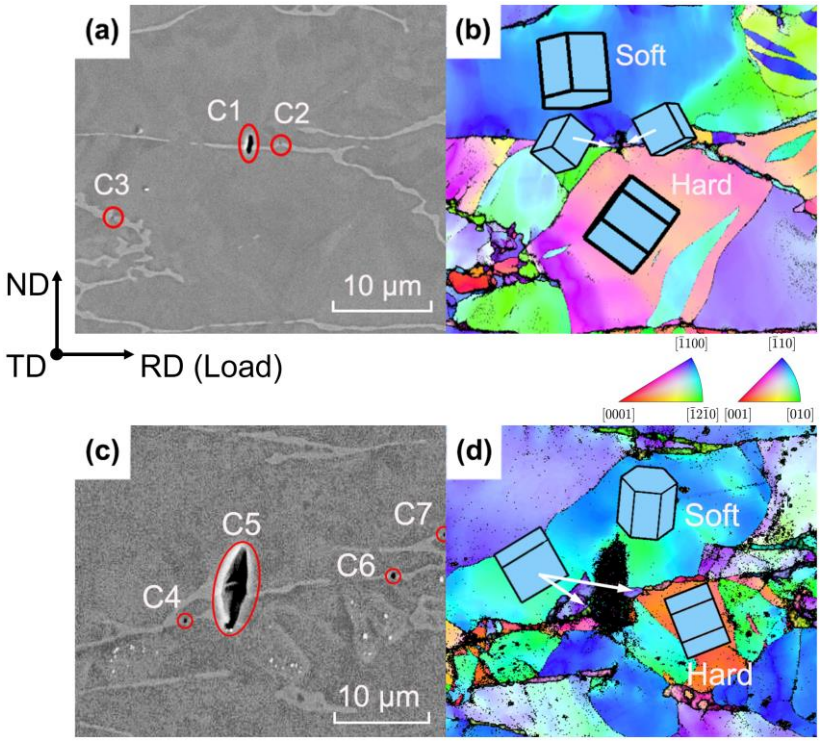

Fig.12 Subsurface cavity nucleation in the intergranular β phase (light region) near two rogue grain combinations. (a) and (c) SEM images, encircled regions indicate the cavities, (b) and (d) corresponding IPF maps of RD.

4.4 Influence of intergranular β phase on dwell fatigue

Experimental studies in the literature generally adopt a dislocation pile-up model proposed by Stroh to explicate the basal facet nucleation under dwell fatigue loading [42]. This analytical model has been verified by crystal plasticity modeling [43], in which the cold creep of soft grains induces stress concentration at the hard-soft grain boundaries during the dwell time span, as shown in the simulated stress σ_{yy} and strain ε_{yy} contours in **Fig. 13(a) and (b)**. The increased grain boundary stress σ_{yy} at the dwell end in turn causes early quasi-cleavage fracture on the basal plane of the hard grain with normal parallel to the loading direction, as shown in **Fig. 13(c)**. However, the intergranular β phase tends to alter the time-dependent dislocation pile-ups at soft-hard grain boundaries in consideration of the slip transfer at the α/β interface (**Fig. 14(a)**), especially for the globular α microstructure that demonstrates no exact orientation relationship between the α and β phases, as illustrated in **Fig. 14(b)**. Thus, the effect of the intergranular β phase on the dwell fatigue behaviors of Ti-Fe-O alloy is characterized in the following sections.

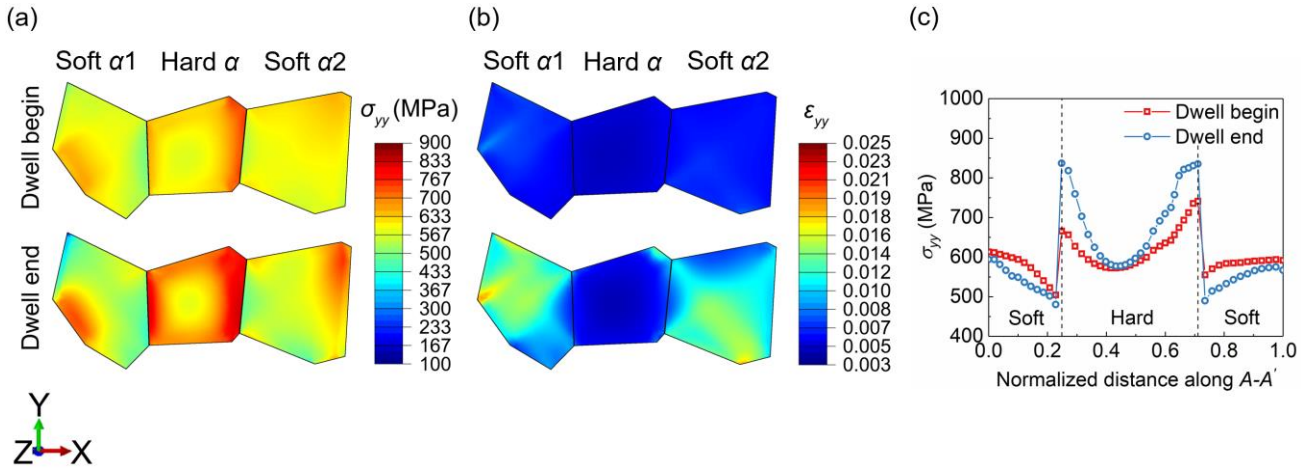

Fig. 13 Simulated (a) stress and (b) strain contours within the rogue grain combination at the beginning and end of the dwell time for the pure α model in Fig. 4, and (c) stress redistribution along the path $A-A'$.

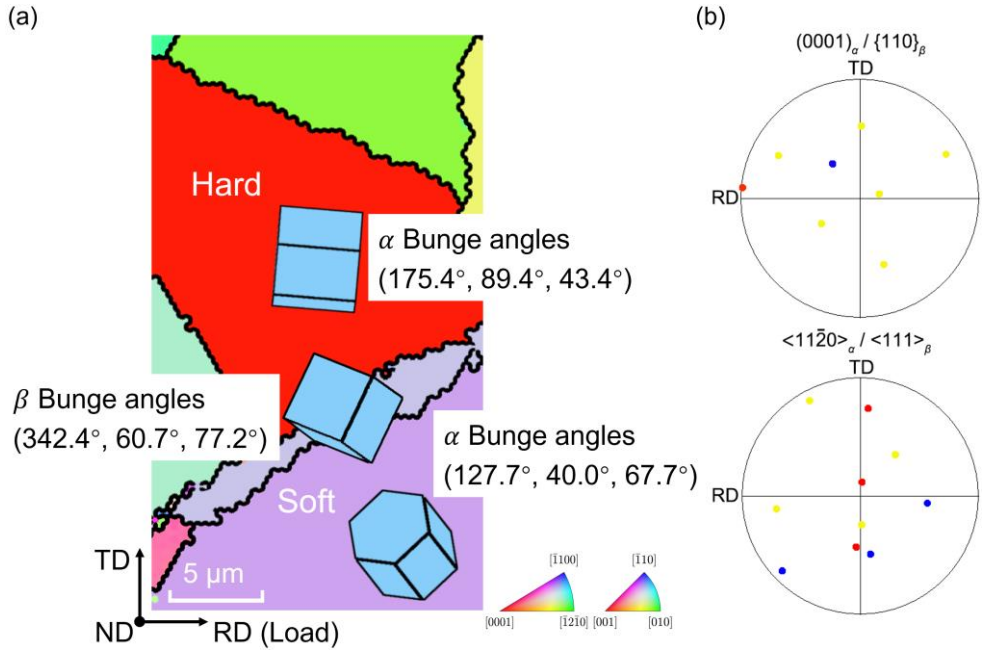

Fig. 14 (a) IPF map of the RD related to a rogue grain combination with the intergranular β lath in Ti-Fe-O alloy, (b) $(0001)_\alpha/\{110\}_\beta$ and $\langle 11\bar{2}0\rangle_\alpha/\langle 111\rangle_\beta$ pole figures of the rogue grain combination. Red, blue and yellow dots represent the orientations for the hard α, soft α and intergranular β lath, respectively.

4.4.1 Slip transfer at the α/β interface

In previous research, various parameters have been proposed to assess the ease of slip transfer at grain boundaries. A geometrical compatibility factor m', developed by Luster and Morris [44], is repeatedly employed:

$$m' = \cos\varphi \cdot \cos\kappa \tag{13}$$

where φ is the angle between the normal factors of the incoming slip plane and the outgoing slip plane, κ is the angle

between incoming and outgoing Burgers vectors. The m' factor ranges from 0 to 1, and the larger the value of m' is, the easier slip can traverse grain boundaries. Besides, the slip transfer also requires a high resolved shear stress on the outgoing slip system. On the basis of aforementioned discussions, five cases are embedded in the soft α-β-hard α grain combination with a thick β lath (**Fig. 5(a)**), as presented in **Fig. 15**. For all cases, the orientations of the soft and hard α grains remain constant, whereas different Bunge Euler angles are given to the sandwiched β lath. As a result, the m' factor, which represents the geometrical compatibility between the prismatic slip (SF=0.5) in soft α grain and the $\langle 111 \rangle$ slip with the highest value of SF in the β lath, lies from 0.11 to 1. The maximum SF of the $\langle 111 \rangle$ slip is set to 0.5 to ensure the occurrence of plastic shear in the β lath and the dominant position of the given slip system on creep deformation in the β lath. The influence of lattice rotation on the SF during creep deformation is ignored because the strain level is low. Concerning the narrow slip length in the β lath and high CRSS for the $\langle 111 \rangle$ slip, the dislocations transmitted from soft α grain presumably dominate the dislocation pile-ups at hard α-β boundary rather than those nucleate in β lath. Therefore, this study mainly focuses on the impact of slip transfer at the α/β interface (i.e., m' factor) on stress redistribution mechanisms. The simulated results of stress redistribution along the path $B-B'$ are plotted in **Fig. 16**. The green dash-dotted line depicts the value of the peak stress after the stress dwell for the pure α structure. Compared to the results of the pure α structure, the stress distributions at the dwell beginning exhibit subtle differences for the five cases, however, the peak stress σ_{yy} in the hard α grain decreases at the dwell end since the insertion of the β lath can interrupt continuous slip, thereby reducing the dislocation pile-ups at the hard α-β boundary. By contrast, the stress rise at the soft α-β boundary is notably greater at the dwell end than that at the dwell beginning. Zhang et al. have reported similar stress difference in stress relaxation tests for Ti-6242 since the β phase is more rate sensitive than the α phase [12]. However, the effect of CRSS difference between the $\langle a \rangle$ slip and $\langle 111 \rangle$ slip on stress redistribution is ignored. Considering the CRSS of the $\langle 111 \rangle$ slip in the β phase is higher than that of the prismatic slip in Ti-Fe-O alloy, the stress concentration in the β lath may also be attributed to dislocation pile-ups at grain boundaries when the slip transfers from low-CRSS slip

systems to high-CRSS slip systems [45], [46]. Given that this CRSS relationship also exists in commercial titanium alloys such as Ti-6242, Ti-6Al-4V and IM834, the stress redistribution between soft α grains and β laths is likely to emerge in a wide range of α/β titanium alloys with equiaxed microstructure [13]. In addition, the σ_{yy} at the soft α-β boundary reduces by 9.4% (from 731 MPa to 662 MPa) with greater m' factor, whereas the peak stress at the hard α-β boundary increases by 4.7% (from 782 MPa to 819 MPa), as shown in **Fig. 17**. As the m' factor increases, the resistance of slip transfer at the soft α-β boundary diminishes and the stress concentration in the β lath is inhibited due to lower dislocation pile-ups in adjacent soft α grain. Meanwhile, smoother slip transmission accelerates the dislocation pile-ups at the hard α-β boundary and promotes the stress change during the stress-hold period. It is also interesting to note that the change in peak stress σ_{yy} at the soft α-β boundary is more sensitive to the m' factor than that at the hard α-β boundary.

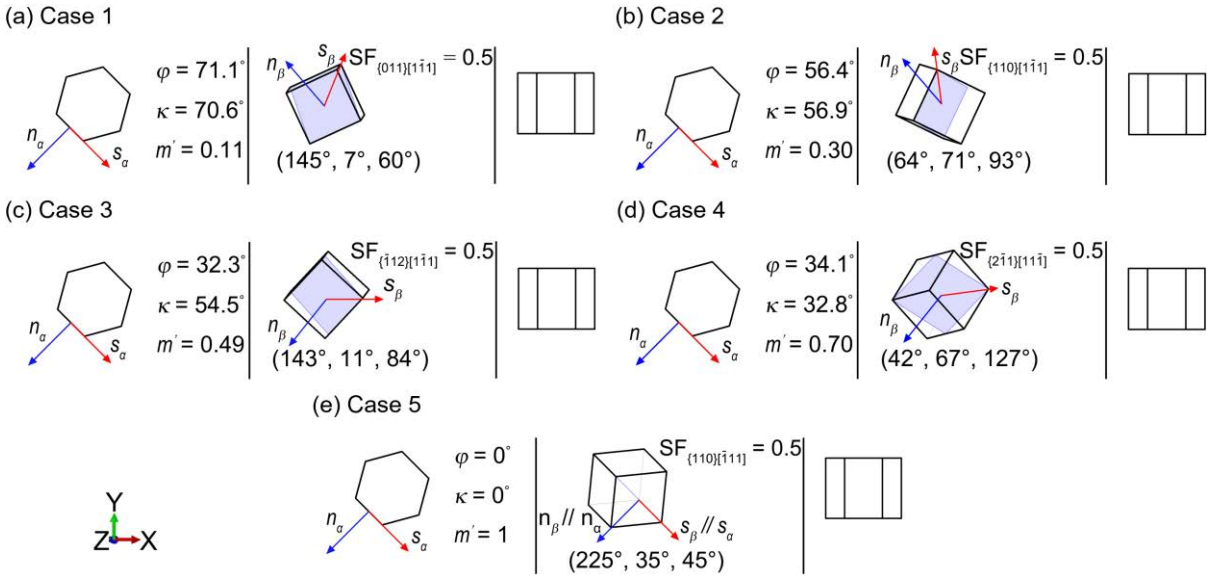

Fig. 15 (a-e) α-β-α grain pair with different orientation relationships. The m' factor represents geometrical compatibility between the prismatic slip (SF = 0.5) and $\langle 111 \rangle$ slip with the highest SF.

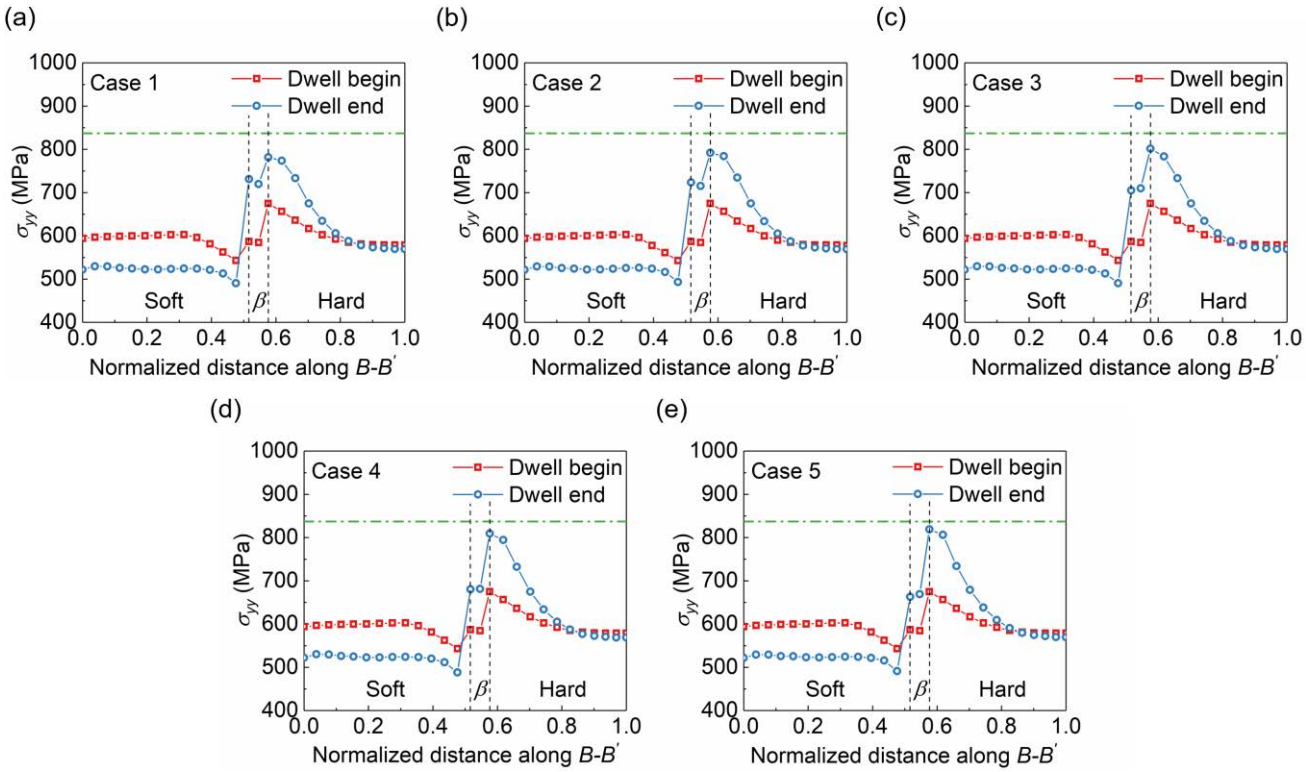

Fig. 16 (a-e) Stress redistribution along the path $B-B'$ for five cases with m' factor ranging from 0.11 to 1. The green dash-dotted line indicates the value of the peak stress after the stress dwell for the pure α structure.

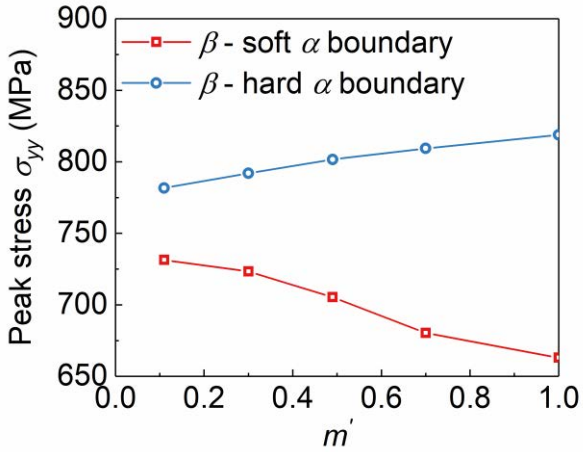

Fig. 17 Relationship between the peak stress and m' factor at dwell end.

The abovementioned numerical results keep consistent with previous CPFE predictions reported by Hamid et al [47] that slip transmission across grain boundaries is easier when misorientation angle between adjacent grains is small. Additionally, the geometrical compatibility between the β lath and abutting soft α grain is confirmed to significantly affect the stress redistribution process during the dwell time. Therefore, the orientation relationship between the β lath

and the two α neighbors in Ti-Fe-O alloy should be characterized. To this end, the angles between the slip plane normal (φ) and slip direction (κ) of most active slip systems within 28 contiguous α/β grain pairs (i.e., 56 α/β grain boundaries) are counted in **Fig. 18(a)-(c)** via EBSD angular calculation. These statistics suggest that over 50% of the $\{10\bar{1}0\}/\{110\}$ and $\{10\bar{1}0\}/\{112\}$ planar misorientation angles exceed 60°. Likewise, 53% of the $\langle 11\bar{2}0\rangle/\langle 111\rangle$ direction misorientation angles are greater than 60°. Due to that the prismatic and $\langle 111\rangle$ slip are respectively primary deformation modes in the α and β phase, these misorientation distributions are prone to result in α/β grain boundaries with low geometrical compatibility (low m' factor). These conditions resemble the description in case 1 (**Fig. 15(a)**), which promotes dislocation pile-ups at the α/β interfaces under dwell fatigue loading.

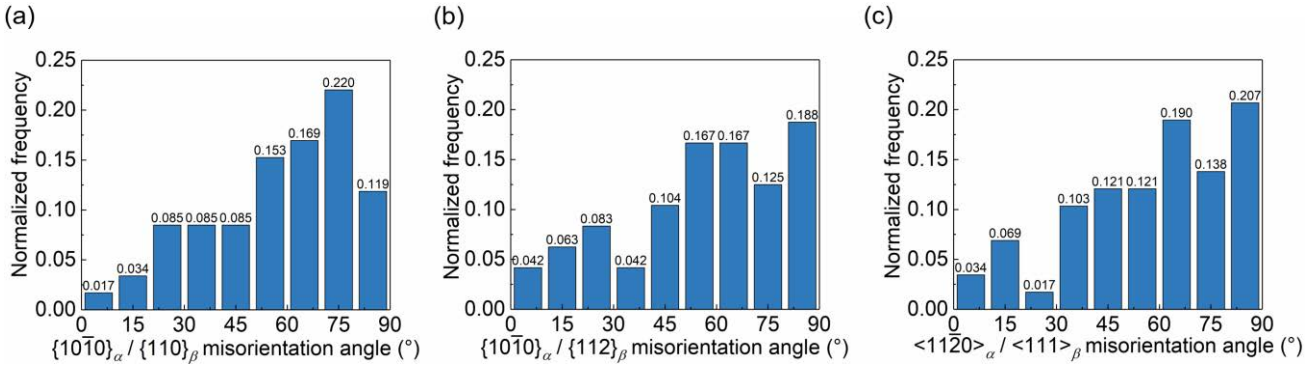

Fig. 18 Misorientation angle distribution between (a) $\{10\bar{1}0\}_\alpha$and $\{110\}_\beta$ planes, (b) $\{10\bar{1}0\}_\alpha$and $\{112\}_\beta$ planes, (c) $\langle 11\bar{2}0\rangle_\alpha$and $\langle 111\rangle_\beta$ directions at α/β interfaces.

4.4.2 β lath thickness

The stress redistribution between hard primary α grains and soft basketweaves with different β lath thicknesses has been evaluated by Zhang et al. and their results reveal that the β lath thickness plays a less important role in inhibiting mobile dislocations than multiple α variants [5]. Motivated by the investigation with respect to the morphological features, the influence of the intergranular β lath thickness on the stress redistribution is examined in this section utilizing models illustrated in **Fig. 5**.

In line with the EBSD measurement, the orientation relationship in case 1 (**Fig. 15(a)**) is adopted for following simulations because it represents the most universal condition in Ti-Fe-O alloy. The stress redistribution process along the

path $B-B^{'}$ is plotted in **Fig. 19(a)** for the thin β lath. The magnitude of the stress change, $\Delta\sigma_{yy}$, is compared with counterparts of the thick β lath and pure α cases, as depicted in **Fig. 19(b)**. The comparison reveals that the redistribution of stress from soft to hard α grain is more inhibited by the thick β lath since sliding dislocations can be halted by more pinning points and the dislocation pile-ups at the hard α-β boundary is reduced. The peak stress at the soft α-β boundary is higher in the thin β lath than in the thick one, which may be attributed to the strong restriction of hard α grain upon the overall creep deformation of the thin β lath. The strain incompatibility between the soft α grain and β lath consequently generates higher grain boundary stress [48]. Additionally, the size-dependent effect with respect to GND accumulation is also involved in local hardening behaviors at small scale (< 10μm) [21]. Thus, the effective density of GNDs along the path $B-B^{'}$ after the dwell period is plotted in **Fig. 20**. The simulated results demonstrate the concentration of GNDs in the β lath, which is consistent with the predictions of Ashton et al. [4]. The decrease in the β lath thickness results in steeper strain gradient and higher effective density of GNDs. Since GNDs can act as obstacles that impede the motion of SSDs and cause work hardening at the grain boundaries, the stresses in the thin β lath and adjacent hard α grain increase from 731 MPa (781 MPa) to 758 MPa (816 MPa) compared to those in the thick one. It should be mentioned that lengthscale-dependent slip transfer mechanisms at the α/β interface have been reported in recent experimental study [46]. According to related observations, the slip from the α phase is inclined to transmit to the slip plane of the β phase that is almost parallel to the incoming plane when the β lath is relatively thin, whereas the slip tends to transfer to the slip system of the β phase with the highest SF when the β lath thickens. To describe the effect of this slip system selection mechanism on the dwell fatigue in α/β titanium alloys, a more integrated crystal plasticity modeling is required.

In summary, thick intergranular β laths can reduce the dwell fatigue sensitivity of α/β titanium alloys with globular structure. Therefore, the reduction of dwell fatigue life debit from Ti-6242 to Ti-6246 with equiaxed structure is not just connected with the disappearance of macrozones and smaller α grain size, the larger volume fraction of the β phase also

plays a crucial role although a high Mo content in the α phase is insufficient to prevent vacancy diffusion induced by the cold creep of soft α grains [49].

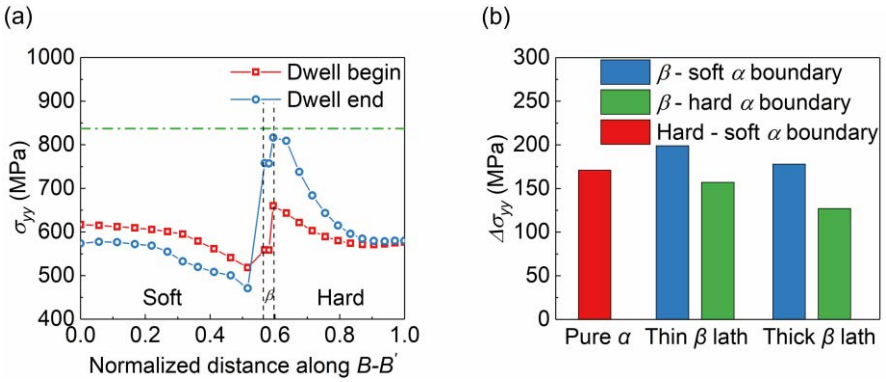

Fig. 19 (a) Stress redistribution along the path $B-B'$ for the thin lath, (b) histogram of the stress change at the grain boundaries for three microstructural morphologies. The green dash-dotted line indicates the value of the peak stress after the stress dwell for the pure α structure.

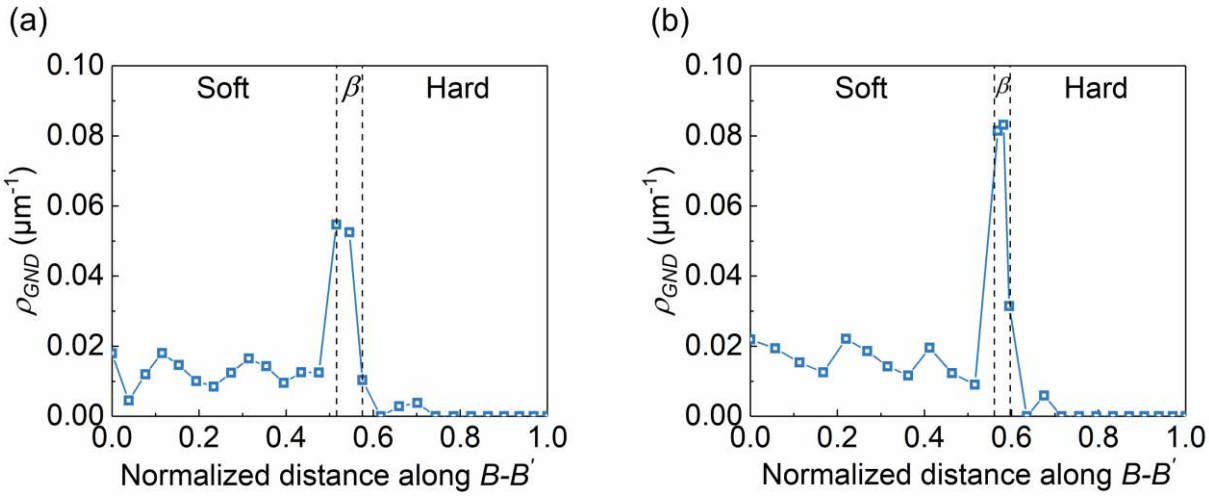

Fig. 20 Distribution of the effective density of GNDs along the path $B-B'$ at the dwell end for the (a) thick β lath, (b) thin β lath.

4.4.3 Maximum stress

In general, early nucleation of basal facets is widely accepted to cause a visible reduction in the time to fracture of titanium alloys under dwell fatigue loading. However, the dwell fatigue fracture mechanism has been reported to convert from facet nucleation to cavity nucleation and coalescence within $\alpha+\beta$ colonies in Ti-6242 when the maximum stress is comparatively high ($\sigma_{max} > 0.92\sigma_y$) [50]. Cavity nucleation is induced by dislocation pile-ups at α/β interfaces even though the BOR relationship is satisfied in the $\alpha+\beta$ colonies. Similarly, the quasi-crack cavities within the β laths

aligned in the loading direction have been identified in Ti-Fe-O alloy (**Fig. 12**) because of the low geometrical compatibility at the α/β interface, and more dislocation pile-ups induced by high $CRSS_{\langle 111\rangle}/CRSS_{prismatic}$ ratio [51]. Inspired by prior works, the influence of the maximum stress on the micromechanical response of the intergranular β phase within a rogue grain combination is further studied.

As the previous section, case 1 with a thick β lath is applied for the crystal plasticity simulation, whilst the maximum stress declines to 538 MPa ($0.85\sigma_y$ at the strain rate of $8.3\times10^{-4}\ s^{-1}$). **Fig. 21** shows the stress redistribution along the path $B-B'$. Compared to the high stress condition, the stress change at the soft α-β boundary decreases from 178 MPa to 89 MPa. The stress increase at the hard α-β boundary drops from 127 MPa to 72 MPa. The peak stress at the soft α-β boundary is 89% of that in the hard α grain, which is smaller than the value (95%) at high stress level. The simulated result indicates that higher stress level can induce more dislocation pile-ups and stress increase at the soft α-β boundary. The increased stress σ_{yy} contributes to the opening stress, which is required for cavity nucleation in the intergranular β lath parallel to the principal load.

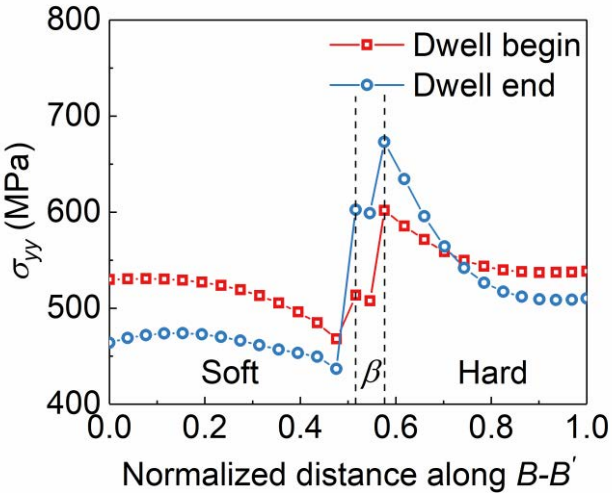

Fig. 21 Stress redistribution along the path $B-B'$ at a maximum stress level of 538 MPa.

Based on the aforementioned numerical predictions at high stress level, the competing mode for crack initiation from basal planes and cavities in the β lath should be considered to comprehensively predict the dwell fatigue life of not only near- α Ti-Fe-O alloy but α/β titanium alloy with globular structure. For crack initiation from basal facets, the

relationship between a proposed effective traction on the basal plane and dislocation density evolution at the soft-hard grain boundary has been constructed to predict the facet nucleation life in equiaxed-structure Ti-6242 alloy [52]. As for the initiation of cracks from cavities in the β lath, the number of dislocations has been adopted as a fatigue indicator parameter (FIP) to predict the cavity nucleation in Ti-6242 alloy with lamellar structure using discrete dislocation dynamics, but the opening stress is not taken into consideration [50]. In accordance with our predicted stress distribution at the dwell end, the opening stress for cavity nucleation in β lath is closer to the peak stress in hard α grain at high stress level. To precisely predict the dwell fatigue crack initiation life for Ti-Fe-O alloy, deduction of a unified FIP available for predicting facet/cavity nucleation and further experimental validation should be carried out to characterize the competing failure modes in the future.

5. Conclusions

The effect of the β phase on the local deformation in the globular α grain structure of Ti-Fe-O alloy is thoroughly investigated under dwell fatigue loading in present paper. The conclusions are summarized as follows:

1. The crystal plasticity parameters of β phase in Ti-Fe-O alloy are determined using nanoindentation tests and crystal plasticity modeling. The slip strength of the β phase is higher than that of the prismatic slip in α phase due to the significant solid solution strengthening of Fe. Reasonable agreements are achieved in predicting the experimental load-displacement, stress-strain and stress relaxation curves.
2. The presence of intergranular β lath within the rogue grain combination inhibits the stress redistribution from the soft to hard α grain. A soft α-β boundary with low geometrical compatibility promotes increased stress in the β lath and further releases the stress concentration in the hard grain during the dwell period.
3. The increase of intergranular β lath thickness is beneficial for reducing the dwell fatigue sensitivity of the α/β titanium alloys with globular structure. Thus, the diminishment of dwell fatigue life debit in Ti-6246 is partly attributed to the high volume fraction of the β phase.

4. A relatively high opening stress for cavity nucleation is developed in the intergranular β lath within the rogue grain combination at high stress state, which may result in two competing premature fracture modes, i.e., basal facet nucleation in the hard α grain and cavity nucleation in the β lath.

The current crystal plasticity predictions with respect to stress redistribution can be extended to a diversity of α/β titanium alloys with globular structure.

Acknowledgement

This paper is supported by ISIJ Research Promotion Grant "Establishment of the principle to design microstructure of ductile two-phase Ti alloys having strong resistance for fracture" within the Iron and Steel Institute of Japan, and by project No. CZ.02.1.01/0.0/0.0/17_049/0008441 "Innovative Therapeutic Methods of Musculoskeletal System in Accident Surgery" within the Operational Programme Research, Development and Education financed by the European Union and by the state budget of the Czech Republic. Yin gratefully thank Dr. Shinichi Takagi at Kanagawa Institute of Industrial Science and Technology for the support in performing nanoindentation tests, Mr. Xiaojin Chen at Bosch (China) Co. Ltd. and Mr. Wentian Zhang at Nanjing University of Aeronautics and Astronautics for the detailed discussion of this work.

Reference

[1]. M.R. Bache. A review of dwell sensitive fatigue in titanium alloys: the role of microstructure, texture and operating conditions. Int J Fatigue 2003;25: 1079-1087. https://doi.org/10.1016/S0142-1123(03)00145-2.

[2]. A.L. Pilchak, J.C. Williams. Observations of facet formation in near-α titanium and comments on the role of hydrogen. Metall Mater Trans A 2011;42: 1000-1027. https://doi.org/10.1007/s11661-010-0507-9

[3]. M.A. Cuddihy, A. Stapleton, S. Williams. On cold dwell facet fatigue in titanium alloy aero-engine components. Int J Fatigue 2017;97: 177-189. https://doi.org/10.1016/j.ijfatigue.2016.11.034.

[4]. P.J. Ashton, T.S. Jun, Z. Zhang, T.B. Britton, A.M. Harte, S.B. Leen, F.P.E. Dunne. The effect of the beta phase on

the micromechanical response of dual-phase titanium alloys. Int J Fatigue 2017;100: 377-387. https://doi.org/10.1016/j.ijfatigue.2017.03.020.

[5]. Z. Zhang, F.P.E. Dunne. Phase morphology, variants and crystallography of alloy microstructures in cold dwell fatigue. Int J Fatigue 2018;113: 324-334. https://doi.org/10.1016/j.ijfatigue.2018.03.030.

[6]. Z. Song, D.W. Hoeppner. Size effect on the fatigue behaviour of IMI 829 titanium alloy under dwell conditions. Int J Fatigue 1989;11.2: 85-90. https://doi.org/10.1016/0142-1123(89)90002-9.

[7]. J. Qiu, Y. Ma, J. Lei, Y. Liu, A. Huang, D. Rugg, R. Yang. A comparative study on dwell fatigue of Ti-6Al-2Sn-4Zr-xMo (x= 2 to 6) alloys on a microstructure-normalized basis. Metall Mater Trans A 2014;45: 6075-6087. https://doi.org/10.1007/s11661-014-2541-5.

[8]. J.R. Seal, M.A. Crimp, T.R. Bieler, C.J. Boehlert. Analysis of slip transfer and deformation behavior across the α/β interface in Ti–5Al–2.5 Sn (wt.%) with an equiaxed microstructure. Mater Sci Eng A 2012;552: 61-68. https://doi.org/10.1016/j.msea.2012.04.114.

[9]. Y. Zhou, K. Wang, Z. Yan, R. Xin, S. Wei, X. Wang, Q. Liu. Ex-situ study on mechanical properties and deformation mechanism of three typical microstructures in TA19 titanium alloy. Mater Charact 2020;167: 110521. https://doi.org/10.1016/j.matchar.2020.110521.

[10]. X.H. Min, L. Zhang, K. Sekido, T. Ohmura, S. Emura, K. Tsuchiya, K. Tsuzaki. Strength evaluation of α and β phases by nanoindentation in Ti–15Mo alloys with Fe and Al addition. Mater Sci Tech 2012;28.3: 342-347. https://doi.org/10.1179/1743284711Y.0000000052.

[11]. T.S. Jun, D.E.J. Armstrong, T.B. Britton. A nanoindentation investigation of local strain rate sensitivity in dual-phase Ti alloys. J Alloy Comp 2016;672: 282-291. https://doi.org/10.1016/j.jallcom.2016.02.146

[12]. Z. Zhang, T.-S. Jun, T.B. Britton, F.P.E. Dunne. Determination of Ti-6242 α and β slip properties using micro-pillar test and computational crystal plasticity. J Mech Phys Solid 2016;95: 393-410.

https://doi.org/10.1016/j.jmps.2016.06.007.

[13]. S. Hémery, P. Villechaise, D. Banerjee. Microplasticity at room temperature in α/β titanium alloys. Metall Mater Trans A 2020;51: 4931-4969. https://doi.org/10.1007/s11661-020-05945-4.

[14]. J. Stráský, P. Harcuba, K. Václavová, K. Horváth, M. Landa, O. Srba, M. Janeček. Increasing strength of a biomedical Ti-Nb-Ta-Zr alloy by alloying with Fe, Si and O. J Mech Behav Biomed Mater 2017;71: 329-336. https://doi.org/10.1016/j.jmbbm.2017.03.026.

[15]. H. Fujii, T. Maeda. Titanium alloys developed by Nippon steel & Sumitomo metal corporation. Nippon Steel & Sumitomo Metal Tech Rep 2014;106: 16-21.

[16]. F. Bachmann, R. Hielscher, H. Schaeben. Texture analysis with MTEX – free and open source software toolbox. Solid State Phenom 2010;160: 63-68. https://doi.org/10.4028/www.scientific.net/SSP.160.63.

[17]. B.N. Lucas, W.C. Oliver. Indentation power-law creep of high-purity indium. Metall Mater Trans A 1999;30: 601–610. https://doi.org/10.1007/s11661-999-0051-7.

[18]. Y. Huang. A User-Material Subroutine Incroporating Single Crystal Plasticity in the ABAQUS Finite Element Program, Harvard Univ, 1991.

[19]. H. Seto, H. Takebe, K. Takahashi, H. Fujii, K. Mori. Effects of oxygen concentration and grain size on twinning deformation behavior in commercially pure titanium, Proc 13th World Conf on Titanium (Ti-2015), San Diego, John Wiley and Sons, Hoboken, NJ. 2016; 1167-1170. https://doi.org/10.1002/9781119296126.ch198.

[20]. X. Liu, Y. Qian, Q. Fan, Y. Zhou, X. Zhu, D. Wang. Plastic deformation mode and α/β slip transfer of Ti–5Al-2.5 Cr-0.5 Fe-4.5 Mo–1Sn–2Zr–3Zn titanium alloy at room temperature. J Alloy Comp 2020;82: 154209. https://doi.org/10.1016/j.jallcom.2020.154209.

[21]. F.P.E. Dunne, D. Rugg, A. Walker. Lengthscale-dependent, elastically anisotropic, physically-based hcp crystal plasticity Application to cold-dwell fatigue in Ti alloys. Int J Plast 2007;23: 1061-1083. https://doi.org/10.1016/j.ijplas.2006.10.013.

[22]. C. Han, H. Gao, Y. Huang, W.D. Nix. Mechanism-based strain gradient crystal plasticity—I. Theory. J Mech Phys Solid 2005;53: 1188-1203. https://doi.org/10.1016/j.jmps.2004.08.008.

[23]. W.B. Lee, Y.P. Chen. Simulation of micro-indentation hardness of FCC single crystals by mechanism-based strain gradient crystal plasticity. Int J Plast 2010;26: 1527-1540. https://doi.org/10.1016/j.ijplas.2010.01.011.

[24]. S. Graff, W. Brocks, D. Steglich. Yielding of magnesium: From single crystal to polycrystalline aggregates. Int J Plast 2007;23: 1957-1978. https://doi.org/10.1016/j.ijplas.2007.07.009.

[25]. G.I. Taylor. The mechanism of plastic deformation of crystals. Part I.—Theoretical. Proc R Soc Lond A 1934;145: 362-387. http://doi.org/10.1098/rspa.1934.0106.

[26]. E.P. Busso, F.T. Meissonnier, N.P. O'dowd. Gradient deformation of two-phase single crystal. J Mech Phys Solid 2000;48: 2333-2361. https://doi.org/10.1016/S0022-5096(00)00006-5.

[27]. M.A. Groeber, M.A. Jackson. DREAM.3D: A Digital Representation Environment for the Analysis of Microstructure in 3D. Integr Mater Manuf I 2014;3: 56-72. https://doi.org/10.1186/2193-9772-3-5.

[28]. J. Zhao, L.X. Lv, G. Liu, K. Wang. Analysis of deformation inhomogeneity and slip mode of TA15 titanium alloy sheets during the hot tensile process based on crystal plasticity model. Mater Sci Eng A 2017;707: 30-39. https://doi.org/10.1016/j.msea.2017.08.094.

[29]. M. Zhang, J. Li, B. Tang, H. Kou, J. Fan. Mechanical characterization and strain-rate sensitivity measurement of Ti-7333 alloy based on nanoindentation and crystal plasticity modeling. Prog Nat Sci 2018;28.6: 718-723. https://doi.org/10.1016/j.pnsc.2018.10.003.

[30]. Z. Zhang. Microscale crystal slip and macroscopic cold creep transition in dwell fatigue. Int J Fatigue 2021;142:

105967. https://doi.org/10.1016/j.ijfatigue.2020.105967.

[31]. J.Y. Kim and S.I. Rokhlin. Determination of elastic constants of generally anisotropic inclined lamellar structure using line-focus acoustic microscopy. J Acoust Soc Am 2009;126: 2998-3007. https://doi.org/10.1121/1.3245032.

[32]. H. Yokoyama, O. Umezawa, K. Nagai, T. Suzuki, K. Kokubo. Cyclic deformation, dislocation structure, and internal fatigue crack generation in a Ti-Fe-O alloy at liquid nitrogen temperature. Metall Mater Trans A 2000;31: 2793-2805. https:// doi.org/10.1007/BF02830339.

[33]. J. Ren, Q. Wang, X. Lu, W. Liu, P. Zhang, X. Zhang. Effect of oxygen content on active deformation systems in pure titanium polycrystals. Mater Sci Eng A 2018;731: 530–538. https://doi.org/10.1016/j.msea.2018.06.083.

[34]. M. Morita, S. Suzuki, Y. Kato, W. Li, O. Umezawa. Tensile deformation of texture-controlled titanium with high oxygen content at room temperature. Mater Sci Eng A 2020;793: 139660. https://doi.org/10.1016/j.msea.2020.139660.

[35]. D. Kang, K. Lee, E. Kwon. Variation of work hardening rate by oxygen contents in pure titanium alloy. Mater Sci Eng A 2015;632: 120-126. https://doi.org/10.1016/j.msea.2015.02.074.

[36]. D.V. Louzguine-Luzgin. High-strength Ti-based alloys containing Fe as one of the main alloying elements. Mater Trans 2018;59: 1537–1544. https://doi.org/10.2320/matertrans.M2018114.

[37]. M. Demiral, A. Roy, V.V. Silberschmidt. Indentation studies in b.c.c. crystals with enhanced model of strain-gradient crystal plasticity. Comput Mater Sci 2013;79: 896-902. https://doi.org/10.1016/j.commatsci.2013.06.057.

[38]. Y. Xu, S. Joseph, P. Karamched, K. Fox, D. Rugg, F.P.E. Dunne, D. Dye. Predicting dwell fatigue life in titanium alloys using modelling and experiment. Nat Commun 2020;11(1): 1-13. https://doi.org/10.1038/s41467-020-19470-w.

[39]. F. Han, B. Tang, H. Kou, J. Li, Y. Feng. Experiments and crystal plasticity finite element simulations of nanoindentation on Ti-6Al-4V alloy. Mater Sci Eng A 2015;625: 28-35. https://doi.org/10.1016/j.msea.2014.11.090.

[40]. K. Kapoor, P. Ravi, R. Noraas, J.S. Park, V. Venkatesh, M.D. Sangid. Modeling Ti–6Al–4V using crystal plasticity, calibrated with multi-scale experiments, to understand the effect of the orientation and morphology of the α and β phases on time dependent cyclic loading. J Mech Phys Solid 2021;146: 104192. https://doi.org/10.1016/j.jmps.2020.104192.

[41]. O. Umezawa, T. Yuasa, W. Li. Fractographical analyses of crack initiation site in high-cycle fatigue for Ti–Fe–O alloy at low temperature. ISIJ Int 2018; 58: 1332-1340. https://doi.org/10.2355/isijinternational.ISIJINT-2017-673.

[42]. A.N. Stroh. The formation of cracks as a result of plastic flow. P Roy Soc Lond.A Mat 1954;223: 404-414. https://doi.org/10.1098/rspa.1954.0124.

[43]. V. Hasija, S. Ghosh, M.J. Mills, D.S. Joseph. Deformation and creep modeling in polycrystalline Ti–6Al alloys. Acta Mater 2003;51: 4533-4549. https://doi.org/10.1016/S1359-6454(03)00289-1.

[44]. J. Luster, M.A. Morris. Compatibility of deformation in two-phase Ti- Al alloys: Dependence on microstructure and orientation relationships. Metall Mater Trans A 1995;26: 1745-1756. https://doi.org/10.1007/BF02670762.

[45]. S. Hémery, P. Nizou, P. Villechaise. In situ SEM investigation of slip transfer in Ti6Al-4V: effect of applied stress. Mater Sci Eng A 2018;709: 277-284. https://doi.org/10.1016/j.msea.2017.10.058.

[46]. D. He, J. Zhu, S. Zaefferer, D. Raabe. Effect of retained beta layer on slip transmission in Ti–6Al–2Zr–1Mo–1V near alpha titanium alloy during tensile deformation at room temperature. Mater Des 2014;56: 937-942. https://doi.org/10.1016/j.matdes.2013.12.018.

[47]. M. Hamid, H. Lyu, B.J. Schuessler, P.C. Wo, H.M. Zbib. Modeling and characterization of grain boundaries and slip transmission in dislocation density-based crystal plasticity. Crystals 2017;7.6: 152. https://doi.org/10.3390/cryst7060152.

[48]. L. Yin, O. Umezawa. Heterogeneous deformation in a commercially pure titanium sheet under dwell fatigue loading: crystal plasticity modeling and experiment. ISIJ Int 2021; ISIJINT-2020-702.

https://doi.org/10.2355/isijinternational.ISIJINT-2020-702.

[49]. A.J. Ready, P.D. Haynes, B. Grabowski, D. Rugg, A.P. Sutton. The role of molybdenum in suppressing cold dwell fatigue in titanium alloys. Proc R Soc A Math Phys Eng Sci 2017;473: 20170189. https://doi.org/10.1098/rspa.2017.0189.

[50]. P. Lefranc, V. Doquet, M. Gerland, C. Sarrazin-Baudoux. Nucleation of cracks from shear-induced cavities in an alpha/beta titanium alloy in fatigue, room-temperature creep and dwell-fatigue. Acta Mater 2008;56: 4450-4457. https://doi.org/10.1016/j.actamat.2008.04.060.

[51]. W. Li, O. Umezawa, N. Koga. Analysis of Subsurface Fatigue Crack Generation in Ti–Fe–O Alloy at Low Temperature. ISIJ Int 2018;58.2: 359-363. https://doi.org/10.2355/isijinternational.ISIJINT-2017-514.

[52]. K. Kirane, S. Ghosh. A cold dwell fatigue crack nucleation criterion for polycrystalline Ti-6242 using grain-level crystal plasticity FE model. Int J Fatigue 2008;30: 2127-2139. https://doi.org/10.1016/j.ijfatigue.2008.05.026.